



# Crystal structure determination and reaction pathway of amide–hydride mixtures

Job Rijssenbeek<sup>a,\*</sup>, Yan Gao<sup>a</sup>, Jonathan Hanson<sup>b</sup>, Qingzhen Huang<sup>c</sup>,  
Camille Jones<sup>c,1</sup>, Brian Toby<sup>c</sup>

<sup>a</sup> GE Global Research, One Research Circle, Niskayuna, NY 12309, United States

<sup>b</sup> Department of Chemistry, Brookhaven National Laboratory, Upton, NY 11973, United States

<sup>c</sup> NIST Center for Neutron Research, 100 Bureau Drive, National Institute of Standards and Technology, Gaithersburg, MD 20899, United States

Received 4 July 2006; accepted 1 December 2006

## Abstract

Combined synchrotron in situ X-ray diffraction and neutron diffraction studies were performed on 2:1 mixtures of lithium amide and magnesium hydride, which have shown promise as solid-state hydrogen storage materials. The dehydrogenated product is a mixed lithium and magnesium imide,  $\text{Li}_2\text{Mg}(\text{NH})_2$ , whose crystal structure has not heretofore been determined. Furthermore, at elevated temperatures,  $\text{Li}_2\text{Mg}(\text{NH})_2$  undergoes two structural transitions from an orthorhombic structure to a primitive cubic structure at intermediate temperature (350 °C) followed by a face-centered cubic crystal structure at high temperature (500 °C). Disordering of the Li, Mg and cation vacancies as a function of temperature drives the structural transitions. We report the reaction pathway from in situ X-ray diffraction studies and the crystal structures of the three structural variants of  $\text{Li}_2\text{Mg}(\text{NH})_2$  as determined by high-resolution X-ray and neutron powder diffraction. We also report the hydrogen storage reaction pathways for mixtures with other cation ratios.

© 2006 Elsevier B.V. All rights reserved.

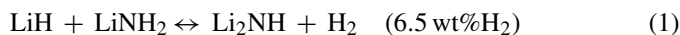
**Keywords:** Hydrogen storage materials; Crystal structure; Order–disorder effects; X-ray diffraction; Neutron diffraction

## 1. Introduction

The lack of practical on-board vehicular hydrogen storage technologies is currently a major barrier to the commercial realization of the hydrogen economy [1,2]. Solid-state storage, such as absorption of hydrogen by metals to form metal hydrides, offers several attractive potential advantages (design flexibility, consumer acceptance, low energy use, etc.) over today's technologies of compressed and liquefied hydrogen. However, most metal hydrides suffer from at least one of two major drawbacks: low hydrogen contents by weight (<3 wt%) and/or high desorption temperatures (>100 °C). Despite a growing worldwide research effort, none of today's hydrogen storage materials are able to simultaneously overcome both of these obstacles. Tackling the enormously challenging problem of practical hydrogen

storage will require new approaches that move beyond the realm of traditional metal hydrides.

One such novel concept, reported by Chen et al. in 2002, is reversible hydrogen storage in a mixture of LiH and  $\text{LiNH}_2$  (reaction (1)) [3,4]. Although the chemistry of this reaction has been known for nearly a century [5], the storage of hydrogen as *both* a hydride (in LiH) and a proton (in  $\text{LiNH}_2$ ) opened a new avenue to lightweight solid-state hydrogen storage:



Unfortunately, this system requires a temperature of >250 °C to achieve an equilibrium hydrogen pressure of 1 atm [3,6]—a temperature which is too high for vehicular applications. In an effort to lower the equilibrium temperature and/or raise the equilibrium pressure, several groups investigated cation substitutions in this system (in the form of varying ratios of  $\text{MgH}_2$  or  $\text{Mg}(\text{NH}_2)_2$ ) and discovered the onset of hydrogen desorption at temperatures as low as 150 °C while still delivering upwards of 5 wt%  $\text{H}_2$  [6–9]. By analogy to reaction (1), Luo [6] chose a 2:1 ratio of  $\text{LiNH}_2$  and  $\text{MgH}_2$  and suggested the following hydrogen

\* Corresponding author. Tel.: +1 518 387 5335; fax: +1 518 387 5595.

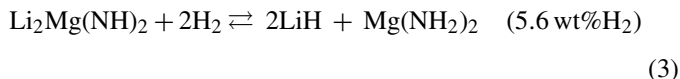
E-mail address: rijssenb@research.ge.com (J. Rijssenbeek).

<sup>1</sup> Current address: Chemistry Department, Hamilton College, Clinton, NY 13323, United States.

release reaction:



As noted in subsequent reports [7–10], the original starting materials are not returned upon rehydrogenation. Instead, hydrogenation and subsequent cycling proceeds via reaction (3):



To our knowledge, the crystal structure of  $\text{Li}_2\text{Mg}(\text{NH})_2$  has not been reported previously, although a cubic unit cell ( $a \approx 10 \text{ \AA}$ ) was postulated by Xiong et al. [8,11]. Given the much improved hydrogen desorption temperatures and equilibrium pressures of the Li–Mg–N–H system, a more profound knowledge of the imide structure and reactivity should help optimize the characteristics of this interesting system. Despite intense research, very little has been published about the reaction pathway(s) and the structure of the dehydrogenation products. We studied the Li–Mg–N–H system using in situ X-ray diffraction for its ability to observe phase changes, crystal structure and crystallite size throughout a reaction in real time. Herein, we report in situ studies of the hydrogen desorption and absorption reactions using combined time-resolved synchrotron X-ray diffraction (XRD) and mass spectrometry (MS); and the structural determination of  $\text{Li}_2\text{Mg}(\text{NH})_2$  at temperatures up to  $500 \text{ }^\circ\text{C}$  by high-resolution synchrotron X-ray diffraction and neutron powder diffraction.

## 2. Experimental

All materials are air and moisture sensitive; therefore all handling was performed in an argon-filled glove box in which the  $\text{O}_2$  and water contents were kept below 1 ppm. Lithium amide ( $\text{LiNH}_2$ ; Aldrich;  $\geq 95\%$  pure) [12], lithium hydride ( $\text{LiH}$ ; Aldrich;  $\geq 95\%$ ), magnesium hydride ( $\text{MgH}_2$ ; Gelest;  $\geq 95\%$ ) and magnesium powder ( $\text{Mg}$ ; Aldrich;  $99.5\%$ ) were used as-received without further purification. Magnesium amide,  $\text{Mg}(\text{NH}_2)_2$ , was synthesized by ammoniation of either magnesium or magnesium hydride powders overnight at  $300 \text{ }^\circ\text{C}$  under 1100 psi (7.6 MPa) ammonia in a high-pressure stainless steel reactor from the Parr Instrument Company. The recovered product was a fine white powder whose X-ray diffraction pattern indicated complete conversion to  $\text{Mg}(\text{NH}_2)_2$ .

All samples were prepared by ball-milling stoichiometric amounts of the reagents in an Argon atmosphere using a Fritsch Pulverisette 4 with tungsten carbide milling jars (80 mL volume) and media ( $\varnothing$  10 mm balls). No catalysts were added. Samples were milled with a 1:15 sample-to-ball weight ratio in cycles of 15 min of milling followed by 3 min of cooling for a total milling time of 8–24 h.

The in situ powder X-ray diffraction was performed at the X7B Beamline of the National Synchrotron Light Source, Brookhaven National Laboratory. X-rays of  $\lambda = 0.922 \text{ \AA}$  were obtained from a Si(1 1 1) monochromator, and were focused to  $0.5 \text{ mm} \times 1 \text{ mm}$  at the sample position by using a bent mirror and a Rh-coated toroidal-focusing mirror. The diffraction patterns were recorded with a Mar345 Image Plate detector, and processed using the program Fit2D [13]. The time-resolved diffraction patterns were taken with  $2\theta_{\text{max}} = 32$  at a rate of one image per minute (20 s exposure and 40 s data readout time).

The in situ sample cell used in the experiment has been previously described in detail [14]. The powder sample was loaded into a 0.5 mm i.d. quartz capillary in an inert atmosphere glove box and the open end was sealed using vacuum grease. For measurement, the quartz capillary was opened just above the sample, quickly placed inside the sapphire tube of the cell and immediately purged with flowing He. Total air exposure was usually less than 5 s. The sample was heated up to  $\sim 500 \text{ }^\circ\text{C}$  with a resistance heater and the temperature was monitored with a

chromel–alumel (K-type) thermocouple placed inside the sapphire capillary and touching the closed end of the sample capillary. During hydrogen desorption, the sample cell was connected to a residual gas analyzer (Stanford Research Systems RGA 200) for real-time qualitative measurement of desorbed gases. For absorption, the cell was isolated from the RGA and operated at up to 2000 psi (13.7 MPa) static hydrogen pressure.

The high-resolution synchrotron X-ray powder diffraction was performed at the X3B1 beamline of the National Synchrotron Light Source, Brookhaven National Lab. X-rays of  $0.6987 \text{ \AA}$  were obtained from a Si(1 1 1) monochromator. The powder sample was loaded under inert atmosphere into a 1.0 mm i.d. quartz capillary and sealed with vacuum grease. The capillary was mounted on a goniometer and was kept in constant rotation to average the crystallite orientation during the data collection. A Ge(1 1 1) analyzer crystal was placed before the scintillation point detector. The data were taken over 15 h between  $5^\circ$  and  $45^\circ$  in  $2\theta$  with  $0.004^\circ$  step size.

The neutron powder diffraction data were collected on both as-desorbed and deuterated samples using the BT-1 high-resolution powder diffractometer at the NIST Center for Neutron Research. Deuterated samples were prepared by performing three absorption/desorption cycles under deuterium gas in a Sieverts' apparatus. A monochromatic neutron beam ( $1.5403 \text{ \AA}$ ) was produced by a Cu(3 1 1) monochromator, with  $90^\circ$  take off angle. Collimators with horizontal divergences of 15, 20, and 7 arcmin were used before and after the monochromator, and after the sample, respectively. About 1.0 g of sample was sealed under inert atmosphere inside a vanadium can about 5 cm high and 0.9 cm in diameter. The diffraction intensities were measured in steps of  $0.05^\circ$  between  $3^\circ$  and  $168^\circ$  in  $2\theta$ . The sample was heated to  $600 \text{ }^\circ\text{C}$  using an ILL-type furnace (ASS Scientific) with a water-cooled aluminum vacuum jacket, dual niobium elements, niobium heat shields, and a niobium sample probe with W/W–30% Re thermocouple.

Temperature programmed desorption (TPD) experiments were performed in a Sieverts' type apparatus (PCTPro-2000 by Hy-Energy Scientific Instruments, LLC). A  $\sim 200 \text{ mg}$  sample of  $2\text{LiNH}_2 + \text{MgH}_2$  was heated to  $250 \text{ }^\circ\text{C}$  at a rate of  $1 \text{ }^\circ\text{C}/\text{min}$  in a known volume initially under vacuum. The pressure generated by the release hydrogen was then converted to  $\text{H}_2$  (wt%) by the following formula:

$$\text{H}_2 \text{ (wt}\%) = \frac{\text{desorbed hydrogen}}{\text{initial weight of sample}} \times 100 \quad (4)$$

The dehydrogenated sample was recharged under 860 psi (5.9 MPa)  $\text{H}_2$  at  $190 \text{ }^\circ\text{C}$  for up to 60 h. After five cycles the sample was heated to  $415 \text{ }^\circ\text{C}$ .

Thermogravimetric analysis (TGA) of the dehydrogenated powder (i.e.,  $\text{Li}_2\text{Mg}(\text{NH})_2$ ) was performed using a TA Instruments TGA2950. The weight change of the sample was measured while heating at  $10 \text{ }^\circ\text{C}/\text{min}$  in a flowing nitrogen atmosphere. The presence of ammonia in the evolved gas stream was checked using damp pH Hydriion paper.

## 3. Results

### 3.1. Hydrogen absorption and desorption cycling

TPD measurements (Fig. 1a) showed the onset of gas release around  $120 \text{ }^\circ\text{C}$  followed by a marked increase above  $150 \text{ }^\circ\text{C}$ . The gas release rate reaches a maximum at  $210 \text{ }^\circ\text{C}$  and was complete by the time the sample reached  $240 \text{ }^\circ\text{C}$ . A total of 5 wt%  $\text{H}_2$  was released, which is less than the theoretical 5.6 wt% but within the expected range given the presence of impurities such as  $\text{MgO}$  and  $\text{Li}_2\text{O}$  in the starting materials. It also assumes that all the desorbed gas is hydrogen. The first desorption (D1) appears to be composed of two gas release processes whereas subsequent cycles (D2–D6) show only a single process. The reversible hydrogen storage capacity varies from 4 to 5 wt%  $\text{H}_2$  depending on the previous absorption time (usually 18 h but as long as 60 h before D4 in Fig. 1a). There was no significant additional gas release upon heating to  $415 \text{ }^\circ\text{C}$  (D6). Absorption is relatively fast during the initial stages but slows significantly

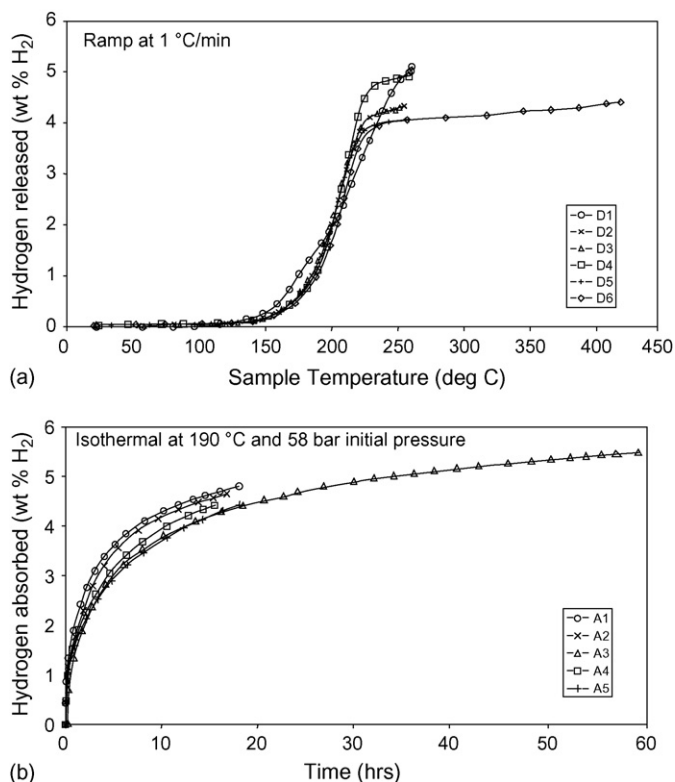


Fig. 1. (a) Hydrogen desorption from an initial mixture of  $2\text{LiNH}_2 + \text{MgH}_2$  into an initially evacuated volume. (b) Hydrogen absorption by  $\text{Li}_2\text{Mg}(\text{NH})_2$  at  $190^\circ\text{C}$  and 860 psi (5.9 MPa) initial hydrogen pressure.

after absorbing  $\sim 2$  wt% (Fig. 1b). This means that an extremely long recharging time ( $>20$  h) is required to achieve consistently high reversible hydrogen storage capacity.

### 3.2. Reaction pathway and phase

In situ X-ray diffraction during hydrogen desorption of the  $2\text{LiNH}_2 + \text{MgH}_2$  mixture (reaction (2)) was performed while heating from  $50$  to  $330^\circ\text{C}$  at  $\sim 12^\circ\text{C}/\text{min}$  while the evolved gases

were monitored by RGA (Fig. 2). The initial patterns confirmed the presence of the  $\text{LiNH}_2$  and  $\text{MgH}_2$  starting materials, along with minor amounts of  $\text{LiH}$ ,  $\text{Li}_2\text{O}$  and  $\text{MgO}$ . The  $\text{LiH}$  is likely the result of some decomposition of the  $\text{LiNH}_2$  during milling. The latter two impurities are present in the as-received starting materials and are extremely difficult to avoid even when these materials are handled in inert atmospheres. At approximately  $280^\circ\text{C}$ , the existing peaks began to weaken and new peaks associated with  $\text{Li}_2\text{Mg}(\text{NH})_2$  first appeared (Fig. 2). Simultaneous RGA measurement revealed that both hydrogen ( $\text{H}_2$  and  $\text{H}$ ) and ammonia ( $\text{NH}_3$ ,  $\text{NH}_2$  and  $\text{N}$ ) were released starting at approximately  $180^\circ\text{C}$ . Both signals peaked at approximately  $280^\circ\text{C}$  after which they dropped off to background levels. The presence of ammonia during the desorption has been reported previously [7,9], and has been implicated in the hydrogen release mechanism [15]. No further changes were observed up to  $330^\circ\text{C}$  and the sample was cooled down to room temperature. The room temperature pattern of  $\text{Li}_2\text{Mg}(\text{NH})_2$  desorbed at  $330^\circ\text{C}$  could be indexed using an orthorhombic unit cell, with space group *Iba2* or *Ibam* and lattice parameters  $a \approx 10 \text{ \AA}$ ,  $b \approx 5 \text{ \AA}$ ,  $c \approx 5 \text{ \AA}$ . For convenience in subsequent discussions, this structure will be referred to as  $\alpha\text{-Li}_2\text{Mg}(\text{NH})_2$  to distinguish it from its structural variants observed at higher temperatures. Interestingly, these parameters are close to those reported by Xiong et al. [11] for a 1:1 ratio of  $\text{LiH}:\text{Mg}(\text{NH}_2)_2$  heated to  $330^\circ\text{C}$  and they observed only a cubic phase for a 2:1 ratio at  $250^\circ\text{C}$ .

For hydrogen absorption,  $\alpha\text{-Li}_2\text{Mg}(\text{NH})_2$  from the previous desorption was heated from  $50$  to  $260^\circ\text{C}$  at  $\sim 12^\circ\text{C}/\text{min}$  under approximately 2000 psi (13.7 MPa)  $\text{H}_2$  pressure (Fig. 3). At  $220^\circ\text{C}$  the peaks associated with  $\alpha\text{-Li}_2\text{Mg}(\text{NH})_2$  weakened while peaks attributable to  $\text{LiH}$  and  $\text{Mg}(\text{NH}_2)_2$  appeared. No further changes were observed up to and while holding at  $330^\circ\text{C}$  indicating complete hydrogen absorption. The mixture of  $\text{LiH}$  and  $\text{Mg}(\text{NH}_2)_2$  was then cooled down to room temperature before the hydrogen was desorbed again. Similar to the desorption of hydrogen from the initial  $\text{LiNH}_2$  and  $\text{MgH}_2$  mixture, peaks associated with  $\alpha\text{-Li}_2\text{Mg}(\text{NH})_2$  appeared at  $210^\circ\text{C}$  as described by (3) (Fig. 4). Although the triplet at  $2\theta = 30^\circ$  is less

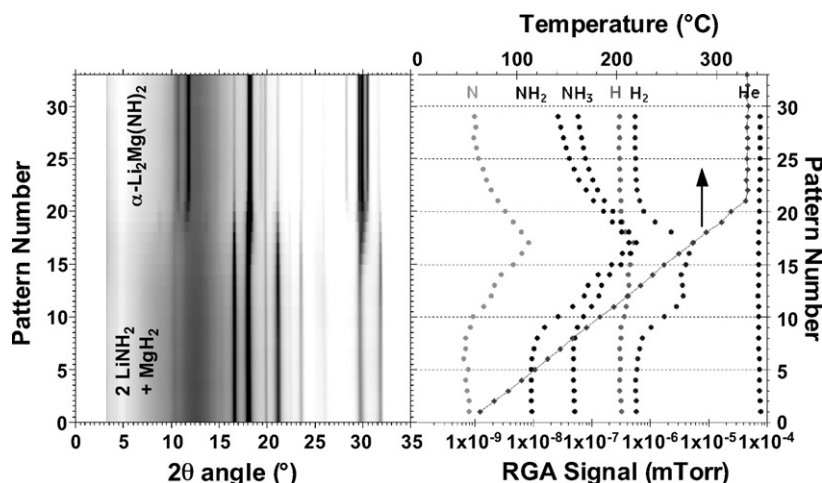


Fig. 2. In situ X-ray diffraction (left) and simultaneous RGA analysis of the evolved gases (right) during the first heating of a mixture of  $2\text{LiNH}_2 + \text{MgH}_2$  to form  $\alpha\text{-Li}_2\text{Mg}(\text{NH})_2$ .

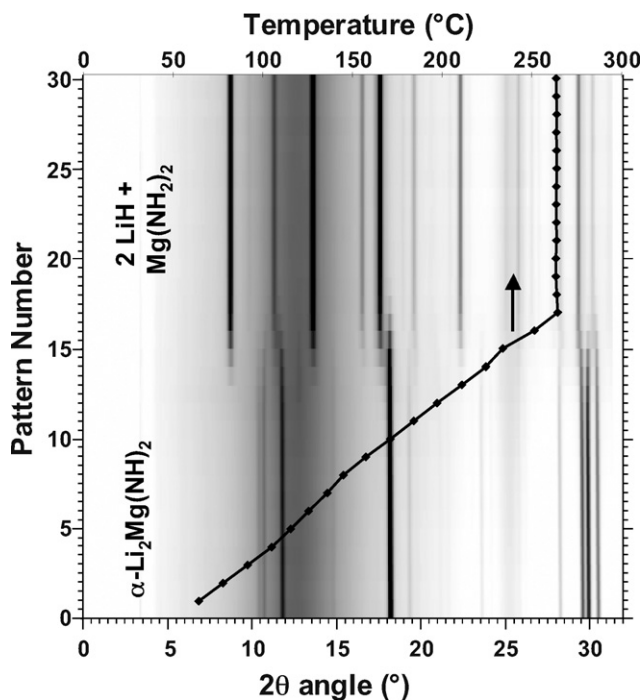


Fig. 3. In situ X-ray diffraction during heating of  $\alpha$ - $\text{Li}_2\text{Mg}(\text{NH})_2$  under approximately 2000 psi (13.7 MPa)  $\text{H}_2$  to form  $\text{Mg}(\text{NH}_2)_2 + 2\text{LiH}$ .

distinct, the two characteristic peaks at  $2\theta \approx 10^\circ$  indicate the return of the orthorhombic structure. Ammonia was detected during this desorption as well, although at significantly lower levels than the first desorption.

As the imide was heated further (to over  $500^\circ\text{C}$  at  $12^\circ\text{C}/\text{min}$ ), two structural phase transitions to higher symmetries were observed (Fig. 5). The first transition started at  $350^\circ\text{C}$ , at which point the orthorhombic  $\alpha$ -phase was gradually replaced by a primitive cubic phase ( $\beta$ - $\text{Li}_2\text{Mg}(\text{NH})_2$ ). The second transition started at  $500^\circ\text{C}$ , during which the primitive cubic phase quickly became face-centered cubic ( $\gamma$ - $\text{Li}_2\text{Mg}(\text{NH})_2$ ). Upon cooling the  $\gamma$ - $\text{Li}_2\text{Mg}(\text{NH})_2$  reverted to  $\beta$ - $\text{Li}_2\text{Mg}(\text{NH})_2$  but the  $\alpha$ - $\text{Li}_2\text{Mg}(\text{NH})_2$  could only be regenerated by cycling under

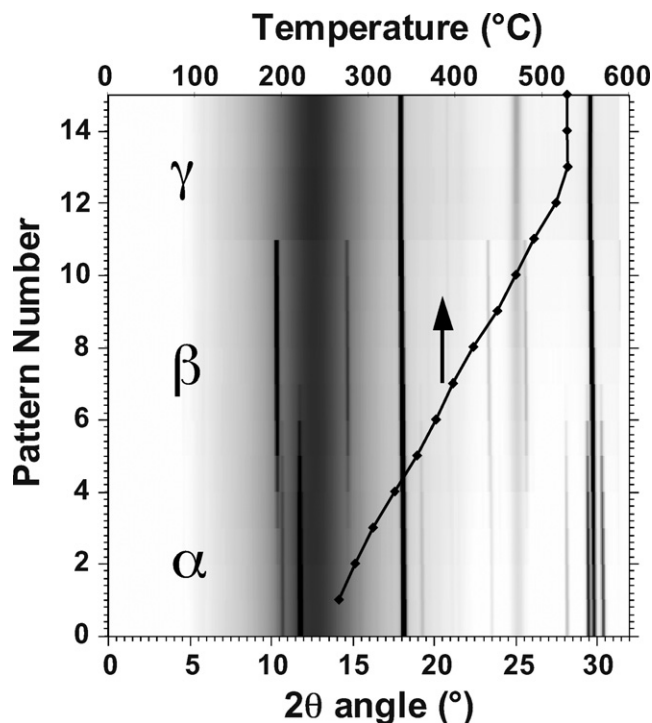


Fig. 5. In situ X-ray diffraction during heating of  $\alpha$ - $\text{Li}_2\text{Mg}(\text{NH})_2$  over  $500^\circ\text{C}$  to form  $\beta$ - $\text{Li}_2\text{Mg}(\text{NH})_2$  starting at  $350^\circ\text{C}$  and  $\gamma$ - $\text{Li}_2\text{Mg}(\text{NH})_2$  at  $500^\circ\text{C}$ .

hydrogen pressure. These high temperature phases will be described in more detail in the sections below. Similar reactions were observed when the starting mixture was  $2\text{LiH} + \text{Mg}(\text{NH}_2)_2$  although the  $\alpha$ - $\text{Li}_2\text{Mg}(\text{NH})_2$  was sometimes difficult to distinguish and the primitive cubic structure appeared at lower temperatures.

TGA, TPD and the combined XRD-MS measurements found that there was a small amount of gas evolution (mainly hydrogen and/or ammonia) over the course of the phase transitions. However, the amount of gas released could not be quantified and the stoichiometric implications of the gas release could not be determined from the diffraction data. The formation of small amounts

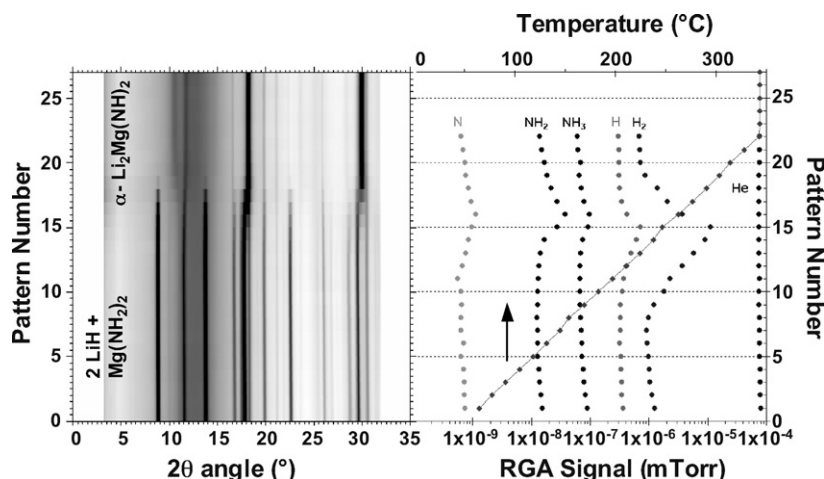


Fig. 4. In situ X-ray diffraction (left) and simultaneous RGA analysis of the evolved gases (right) during the second heating of a mixture of  $\text{Mg}(\text{NH}_2)_2 + 2\text{LiH}$  to form  $\alpha$ - $\text{Li}_2\text{Mg}(\text{NH})_2$ . Note that the ammonia related signals in the RGA are markedly lower than in Fig. 2.

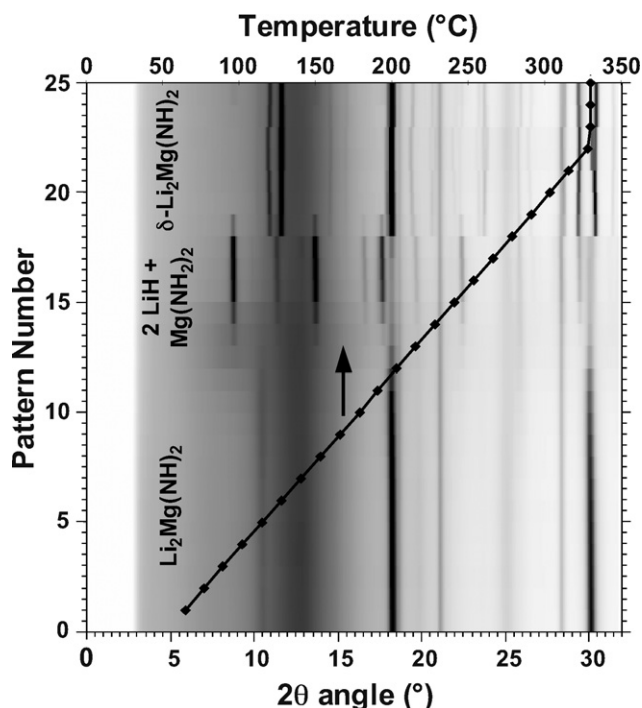


Fig. 6. In situ X-ray diffraction during heating of  $\beta$ - $\text{Li}_2\text{Mg}(\text{NH})_2$  to  $330^\circ\text{C}$  under 2000 psi (13.7 MPa)  $\text{H}_2$ . Initially, hydrogen is absorbed to form  $\text{Mg}(\text{NH})_2 + 2\text{LiH}$  but continued heating re-releases the hydrogen and yields  $\delta$ - $\text{Li}_2\text{Mg}(\text{NH})_2$  at  $290^\circ\text{C}$ .

of  $\text{Mg}_3\text{N}_2$  was observed in some but not all experiments at the highest temperatures. TGA and TPD experiments also revealed that the reversible hydrogen storage capacity was degraded by approximately one third once the sample was heated to  $400^\circ\text{C}$  or above. Therefore, the structural transitions may be accompanied by slight changes in stoichiometry, however the specific nature of the gas(es) evolved and their relationship to the structure is not clear at this juncture.

A fourth structural variant,  $\delta$ - $\text{Li}_2\text{Mg}(\text{NH})_2$ , was observed while under high-pressure hydrogen at high temperatures. Fig. 6 shows the behavior of  $\text{Li}_2\text{Mg}(\text{NH})_2$  when heated under 2000 psi (13.7 MPa)  $\text{H}_2$ . As described above,  $\text{Li}_2\text{Mg}(\text{NH})_2$  absorbed hydrogen to form  $\text{LiH}$  and  $\text{Mg}(\text{NH})_2$  at approximately  $220^\circ\text{C}$ , however at  $290^\circ\text{C}$  this mixture released hydrogen to form  $\delta$ - $\text{Li}_2\text{Mg}(\text{NH})_2$ . The diffraction pattern of  $\delta$ - $\text{Li}_2\text{Mg}(\text{NH})_2$  could be indexed by a tetragonal cell with  $a \approx 5.16 \text{ \AA}$  and  $c \approx 9.60 \text{ \AA}$ , which is very similar to  $\alpha$ - $\text{Li}_2\text{Mg}(\text{NH})_2$ . A structural refinement was not undertaken because, at the time of publication, high-resolution diffraction data were not available for this phase. When the temperature was lowered below  $280^\circ\text{C}$  while maintaining the high hydrogen pressure,  $\delta$ - $\text{Li}_2\text{Mg}(\text{NH})_2$  reverted to  $\text{Mg}(\text{NH})_2$  and  $\text{LiH}$ .

### 3.3. Structure determination of $\alpha$ - $\text{Li}_2\text{Mg}(\text{NH})_2$

An accurate crystal structure determination for  $\alpha$ - $\text{Li}_2\text{Mg}(\text{NH})_2$  required both neutron and X-ray diffraction data. The former yields accurate hydrogen positions while the latter is more sensitive to the mixed Li and Mg cation sites. Data were collected at room temperature on deuterated  $\alpha$ -

$\text{Li}_2\text{Mg}(\text{NH}_{1-x}\text{D}_x)_2$  ( $x \sim 0.7$ ) [16]. The indexing of diffraction patterns, refinement of lattice parameters, and the determination of space group were performed using the Jade analysis software [17]. Based on systematic absences, two space groups are possible: *Iba2* and *Ibam*. Initial structural models were obtained for both space groups by submitting the lattice parameters, space group and expected composition to FOX, a program for ab initio structure determination from powder diffraction data [18]. The output was then refined by the Rietveld method using GSAS [19].

The X-ray data was refined first and the resulting model was subsequently refined against the neutron data. The two data sets could not be refined together because the hydrogen positions as determined by the two methods are not the same. X-rays are scattered by the electrons, which are localized in chemical bonds, whereas neutrons are scattered by the nuclei themselves, therefore the N–H bond length deduced from X-ray data is significantly shorter ( $0.94 \text{ \AA}$ ) than that derived from the neutron ( $0.999 \text{ \AA}$ ). Coincidentally, the neutron experiment is relatively insensitive to the positions and displacement factors of the cations because the neutron scattering lengths of Li and Mg largely cancel each other out when they are present on the same crystallographic site in a 2:1 ratio (total scattering length of  $\sim 0.4 \text{ fm}$ ) [20]. Therefore, the cation positions and displacement factors used in the refinement of the neutron diffraction

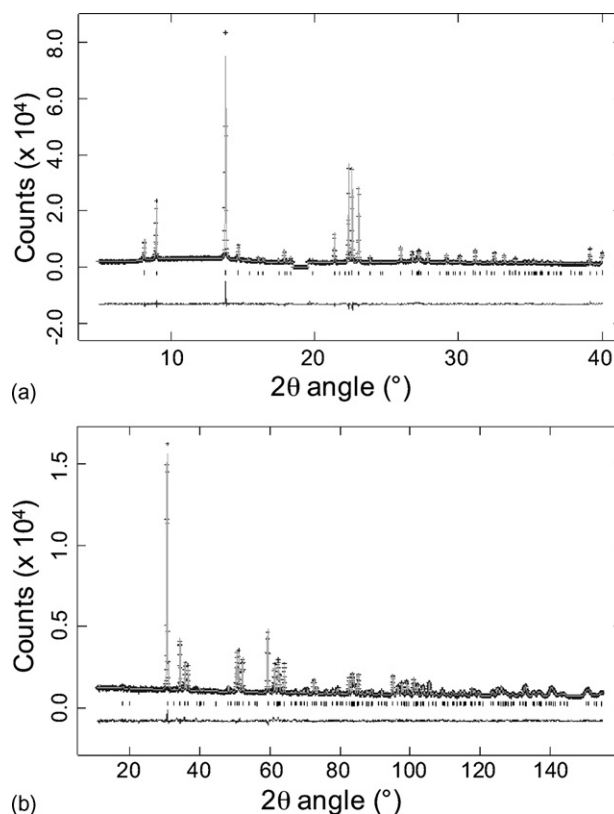


Fig. 7. Rietveld refinement results of the (a) high-resolution synchrotron X-ray and (b) neutron data for the model of  $\alpha$ - $\text{Li}_2\text{Mg}(\text{NH})_2$  in space group *Iba2*. Data (crosses), fitted profile (line), allowed Bragg reflections (tick marks) and difference curve (lower line) are shown. The region around the main peak of  $\text{MgO}$  ( $2\theta \approx 19^\circ$ ) was omitted from the refinement of the X-ray data.

Table 1  
Unit cell and atomic parameters from Rietveld refinement of  $\alpha$ -Li<sub>2</sub>Mg(NH)<sub>2</sub> in space group *Iba2* (no. 45) using high-resolution synchrotron X-ray ( $\lambda = 0.6987 \text{ \AA}$ ) and neutron ( $\lambda = 1.5403 \text{ \AA}$ ) powder diffraction data collected at room temperature

Unit cell parameters		Synchrotron	Neutron
$a$ (Å)		9.7837(1)	9.7871(2)
$b$ (Å)		4.9893(1)	4.9927(1)
$c$ (Å)		5.1984(1)	5.2019(1)
$V$ (Å <sup>3</sup> )		253.75(1)	254.19(1)
$Z$		4	4
Atomic parameters			
N (8c)	$x$	0.1358(1)	0.1357(1)
	$y$	0.2794(2)	0.2785(2)
	$z$	0.0000 <sup>a</sup>	0.0000 <sup>a</sup>
	$U_{\text{iso}}$ (Å <sup>2</sup> )	0.0185(4)	0.0197(4)
	Occupancy	1.000	1.000
Li/Mg(I) (4b)	$x$	0.0000	0.0000
	$y$	0.5000	0.5000
	$z$	0.2577(17)	0.2500 <sup>a</sup>
	$U_{\text{iso}}$ (Å <sup>2</sup> )	0.0127(3)	0.0125 <sup>a</sup>
	Occupancy	0.626(1)/0.374	0.589(5)/0.411
Li/Mg(II) (8c)	$x$	0.2405(1)	0.2500 <sup>a</sup>
	$y$	−0.0054(9)	0 <sup>a</sup>
	$z$	0.7536(11)	0.7500 <sup>a</sup>
	$U_{\text{iso}}$ (Å <sup>2</sup> )	0.0127(3)	0.125 <sup>a</sup>
	Occupancy	0.752(1)/0.248	0.706(3)/0.294
H/D (8c)	$x$	0.0795(11)	0.0644(5)
	$y$	0.1450(24)	0.1427(7)
	$z$	−0.0054(9)	−0.0440(10)
	$U_{\text{iso}}$ (Å <sup>2</sup> )	0.0254(73)	0.0412(18)
	Occupancy	1.00/0 <sup>a</sup>	0.303(8)/0.697
Rietveld refinement statistics <sup>b</sup>			
$R_p$		3.91%	2.97%
$R_{wp}$		5.01%	3.72%
$\chi^2$		2.039	1.491
$R(F^2)$		6.8%	10.55%
No. of Bragg peaks		104	149

<sup>a</sup> Parameters were fixed during refinement.

<sup>b</sup>  $R$ -factors were calculated after background subtraction.

data were fixed at those obtained from the high-resolution X-ray data. The Rietveld refinement results for the model in space group *Iba2* are summarized in Table 1, and the fits of the X-ray and neutron data are given in Fig. 7. To account for geometric effects, a cylindrical absorption correction was applied to the neutron data.

The crystal structure of  $\alpha$ -Li<sub>2</sub>Mg(NH)<sub>2</sub> (Fig. 8) can be described as a supercell of the high temperature cubic form of lithium imide, Li<sub>2</sub>NH [21,22]. The doubling of the  $a$ -axis is the result of ordering of the cation vacancy introduced by the substitution of two Li atoms by a single Mg atom. To illustrate the similarity with Li<sub>2</sub>NH, Li<sub>2</sub>Mg(NH)<sub>2</sub> can be rewritten as LiMg<sub>0.5</sub>□<sub>0.5</sub>NH in which 25% of the tetrahedral cation sites are vacant (□). Although the cation vacancies are ordered, the Li and Mg atoms are randomly distributed over two crystallographically distinct sites (LM1 & LM2) in an approximately 2:1 ratio. This disorder is not unexpected because their ionic radii are nearly identical (0.73 Å versus 0.71 Å) [23].

The H/D ratio in the deuterated sample refined to 30/70 indicating incomplete replacement of H by D during cycling under D<sub>2</sub>. The N site was assumed to be fully occupied, and the occupancy was set to unity and was not refined in either the X-ray or the neutron data. The composition derived from the neutron data is Li<sub>1.95</sub>Mg<sub>1.05</sub>(NH)<sub>2</sub>, whereas it is Li<sub>2.13</sub>Mg<sub>0.87</sub>(NH)<sub>2</sub> in the X-ray refinement. The difference is attributed to the formation of impurities over time in the latter. Although the same material was used for both the PND and HR-XRD experiments, the latter was carried out several weeks after the former, and the detection of oxide phases in the HR-XRD pattern suggests that the sample could have been slightly oxidized during sample handling between the two experiments. The PND data indicated only single-phase  $\alpha$ -Li<sub>2</sub>Mg(NH)<sub>2</sub>, whereas the high-resolution X-ray diffraction measurement contained weak peaks that could be assigned to trace amounts of MgO and LiH (both with a net peak intensity less than 1% of the main peak intensity).

Rietveld refinements were also carried out in space group *Ibam* because it cannot be distinguished from *Iba2* based on

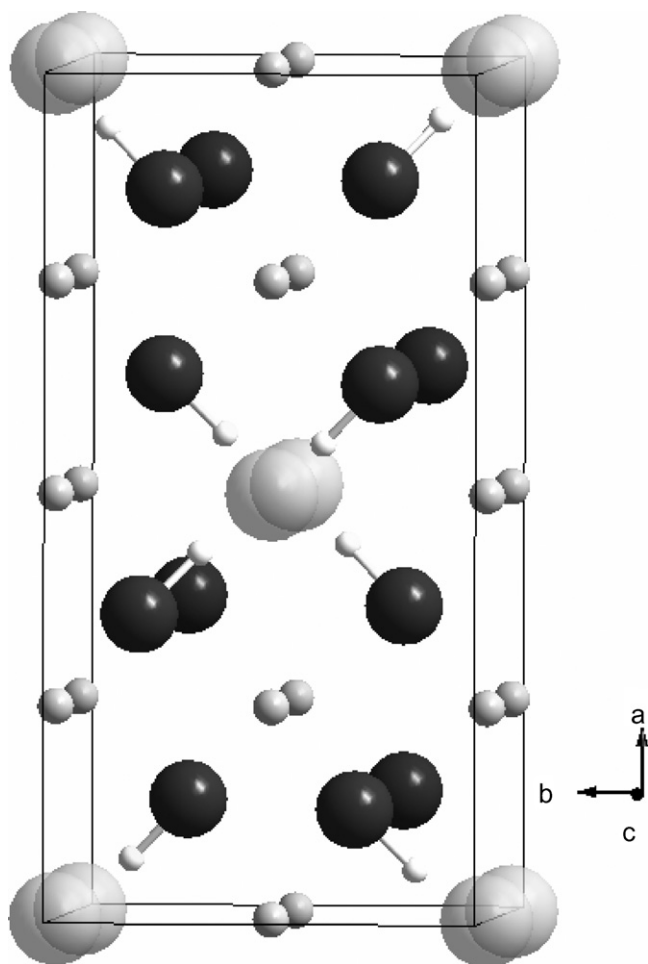
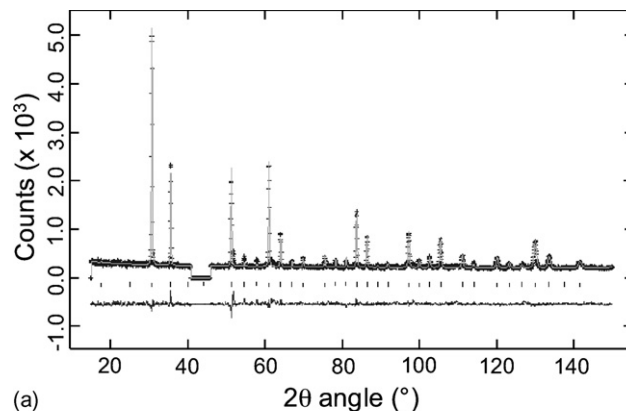


Fig. 8. Structure of  $\alpha$ - $\text{Li}_2\text{Mg}(\text{NH})_2$ . Nitrogen atoms (dark grey), protons (white), mixed lithium and magnesium sites (small light grey) and vacancies (large transparent grey) are shown. Note that the imide protons are associated with the cation vacancies.

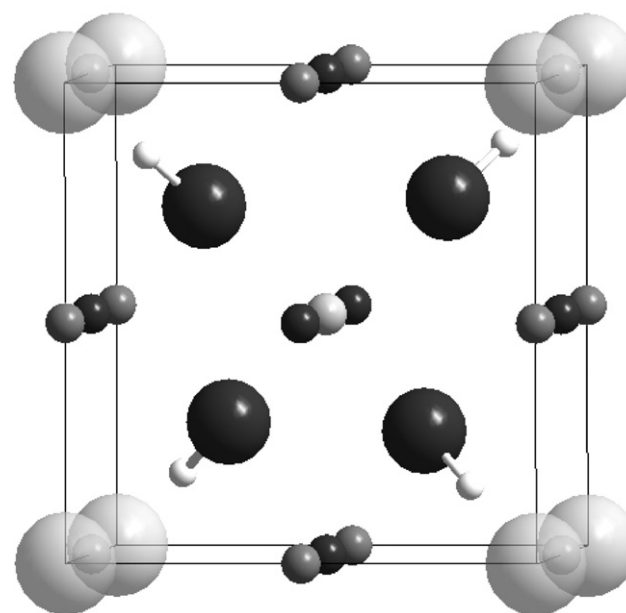
systematic absences. In the *Ibam* refinement, for simplicity N, LM1 and LM2 were placed at special positions 8j, 4b and 8f, respectively. H/D was placed either at a general position (16k) or on the same mirror plane as N (8j). The refinements with H/D on the mirror plane yielded unrealistically short N–H bond lengths and abnormally large displacement factors. When H/D is placed on the general position, it becomes disordered with partial occupancy above and below the mirror plane. Although yielding acceptable bond lengths, the goodness of fit parameters were not significantly different from those of space group *Iba2*. We chose space group *Iba2* for its simplicity with the understanding that the refinement alone cannot exclude the *Ibam* structure with disordered H atoms.

#### 3.4. Structure determination of $\beta$ - $\text{Li}_2\text{Mg}(\text{NH})_2$

$\beta$ - $\text{Li}_2\text{Mg}(\text{NH})_2$  has a primitive cubic unit cell with  $a = 5.0268(1) \text{ \AA}$  and was observed in both the in situ X-ray diffraction measurements (Fig. 5 from 300 to 500 °C) and the neutron diffraction measurement (Fig. 9a). It can be obtained both by heating the  $\alpha$ -phase and by cooling the  $\gamma$ -phase. Xiong



(a)



(b)

Fig. 9. (a) Rietveld refinement results of the neutron data for the model of  $\beta$ - $\text{Li}_2\text{Mg}(\text{NH})_2$  in space group  $P\text{-}4_3m$ . Data (crosses), fitted profile (line), allowed Bragg reflections (tick marks) and difference curve (lower line) are shown. The region around the main peak of MgO ( $2\theta \approx 42^\circ$ ) was omitted from the refinement. (b) Structure of  $\beta$ - $\text{Li}_2\text{Mg}(\text{NH})_2$ . Nitrogen atoms (dark grey), protons (white), lithium (light grey bcc site), two distinct mixed lithium and magnesium sites (small dark grey) and vacancies (large translucent grey) are shown. Note that the imide protons are associated with the cation vacancies now located at the corners of the cubic cell.

et al. also reported a primitive cubic structure for  $\text{Li}_2\text{Mg}(\text{NH})_2$  but with  $a = 10.05 \text{ \AA}$  [11]. We did not observe any evidence for such a large unit cell in either our X-ray or neutron diffraction data. The space group of  $\beta$ - $\text{Li}_2\text{Mg}(\text{NH})_2$  was found to be  $P\text{-}4_3m$ , in which both the (1 0 0) and (1 1 0) low angle reflections are allowed. Using the anti-fluorite structure of  $\text{Li}_2\text{NH}$  as reference, the eight tetrahedral cation sites are divided into four distinct crystallographic sites: bcc sites, fcc sites, corner sites, and edge sites (Fig. 9b). Rietveld refinement of the in situ X-ray data found that Li, Mg, and the vacancies are distributed over these sites in a complex manner, and therefore the overall composition was constrained to be  $\text{Li}_2\text{Mg}(\text{NH})_2$ . Of the four distinct sites, the corner sites are empty, the edge-centered sites are 1/3

Table 2  
Comparison of refinement results for different models of the hydrogen positions in  $\beta$ -Li<sub>2</sub>Mg(NH)<sub>2</sub> in *P*-4<sub>3</sub>*m* (no. 215)

Site occupancy		Bond lengths (Å)			Refinement parameters <sup>a</sup>				
4e	12i	N–H1	N–H2	H <i>U</i> <sub>iso</sub>	<i>R</i> <sub>wp</sub>	<i>R</i> <sub>p</sub>	<i>R</i> ( <i>F</i> <sup>2</sup> )	$\chi^2$	Ref.
0.25	0.25	0.999(7)	1.007(6)	0.057(5)	0.0781	0.0592	0.1196	1.824	48
0.50	0.17	1.000(6)	1.006(6)	0.053(3)	0.0759	0.0579	0.1148	1.724	48
1.00	0.00	0.984(5)	n/a	0.068(4)	0.0758	0.0577	0.1036	1.723	48

<sup>a</sup> *R*-factors were calculated after background subtraction.

Table 3  
Unit cell and atomic parameters from Rietveld refinement of  $\beta$ -Li<sub>2</sub>Mg(NH)<sub>2</sub> in space group *P*-4<sub>3</sub>*m* (no. 215) using neutron powder diffraction data ( $\lambda = 1.5403$  Å) collected at room temperature

Atom/position	<i>x</i>	<i>y</i>	<i>z</i>	<i>U</i> <sub>iso</sub> (Å <sup>2</sup> )	Occupancy
N (4e)	0.2666(2)	0.2666	0.2666	0.0174(4)	1.00
Li (1b)	0.5000	0.50	0.50	0.025	1.00
Li/Mg (I) (3d)	0.5000	0.00	0.00	0.025	0.59(1)/0.08(1)
Li/Mg (II) (3c)	0.0000	0.50	0.50	0.025	0.41/0.59
H/D (4e)	0.1567(8)	0.1567	0.1567	0.057(5)	0.27/0.73(1)

Unit cell parameters: *a* = 5.0268(1) Å; *V* = 127.02(1) Å<sup>3</sup>; *Z* = 2. Rietveld refinement statistics (*R*-factors were calculated after background subtraction): *R*<sub>p</sub> = 5.77%; *R*<sub>wp</sub> = 7.58%;  $\chi^2 = 1.723$ ; *R*(*F*<sup>2</sup>) = 10.36% (48 Bragg peaks).

vacant while the other 2/3 is occupied mainly by Li, the fcc sites are shared by both Li and Mg, and the bcc sites are fully occupied by Li.

The refinement of the room temperature neutron data indicates that there are four H atoms in the unit cell, distributed over two possible positions: one being the 4e position (*x**x**x*), which yields an N–H bond pointing to the vacant corner sites, and another being the 12i position (*x**x**z*), wherein the N–H bond points between the vacant corner site and a partially occupied edge site. These two sites can be populated in one of three possible ways: (1) the four H atoms are at the 4e position, which is similar to the orthorhombic structure of the  $\alpha$ -phase. (2) Two H atoms at the 4e sites and two at the 12i site, since each unit cell has one vacant corner site and one vacant edge site. (3) The H atoms is distributed over the two sites, 4e and 12i, with different ratios such as one H at 4e and three at 12i. These three H distribution models were considered in the refinement (Table 2). The model with all the H atoms at the 4e positions yielded a slightly better fit and is considered the simplest. The Rietveld fit based on this model is illustrated in Fig. 9b and the structural parameters are listed in Table 3.

Table 4  
Unit cell and atomic parameters from Rietveld refinement of  $\gamma$ -Li<sub>2</sub>Mg(NH)<sub>2</sub> in space group *Fm*-3*m* (no. 225) using in situ X-ray data ( $\lambda = 0.922$  Å) collected at ~500 °C

Atom/position	<i>x</i>	<i>y</i>	<i>z</i>	<i>U</i> <sub>iso</sub> (Å <sup>2</sup> )	Occupancy
N (4a)	0.0000	0.0000	0.0000	0.056(4)	1.00
Li/Mg (8c)	0.2500	0.2500	0.2500	0.044(4)	0.55(1)/0.20

Unit cell parameters: *a* = 5.0988(2) Å; *V* = 132.56(1) Å<sup>3</sup>; *Z* = 2. Rietveld refinement statistics (*R*-factors were calculated after background subtraction): *R*<sub>p</sub> = 12.13%; *R*<sub>wp</sub> = 25.98%;  $\chi^2 = 4.209$ ; *R*(*F*<sup>2</sup>) = 3.4% (6 Bragg peaks).

### 3.5. Structure determination of $\gamma$ -Li<sub>2</sub>Mg(NH)<sub>2</sub>

Complete conversion of  $\beta$ -Li<sub>2</sub>Mg(NH)<sub>2</sub> to the  $\gamma$  structure was not achieved in the neutron experiment, therefore the in situ X-ray diffraction pattern obtained at 530 °C was used for the structural refinement. Because of its strong resemblance to that reported for high temperature Li<sub>2</sub>NH [21,22,24], the pattern was indexed using a face-centered cubic cell with space group *Fm*-3*m* and *a* ≈ 5 Å (Table 4) [25]. Subsequent Rietveld refinement (Fig. 10a) indicated that the Li and Mg atoms, and vacancies are randomly distributed over the tetrahedral sites in a 2:1:1 ratio. As in Li<sub>2</sub>NH, the N atoms occupy the fcc sites and the Li atoms the tetrahedral sites (Fig. 10b). Although the positions of the imide protons could not be determined from the in situ X-ray data, comparison to the  $\alpha$  and  $\beta$  structures suggests that they are in the 32f site (one-eighth occupied) and associated with the vacancies in the tetrahedral sites.

## 4. Discussion

The elucidation of the various crystal structures of Li<sub>2</sub>Mg(NH)<sub>2</sub> has shed light on the hydrogen storage properties of the entire Li–Mg–N–H system. It is worthwhile to begin the discussion by comparing the structure of  $\alpha$ -Li<sub>2</sub>Mg(NH)<sub>2</sub> to those of Li<sub>2</sub>NH and LiNH<sub>2</sub>. All three are derived from the anti-fluorite structure-type with the cations (Li<sup>+</sup> and/or Mg<sup>2+</sup>) in tetrahedral sites and the anions (NH<sub>2</sub><sup>2-</sup> or NH<sub>2</sub><sup>-</sup>) in cubic sites. In  $\alpha$ -Li<sub>2</sub>Mg(NH)<sub>2</sub>, the ordering of the cation vacancies created by substitution of two Li<sup>+</sup> by a single Mg<sup>2+</sup> yields an orthorhombic unit cell roughly twice the size of the cubic Li<sub>2</sub>NH cell (Fig. 11a and b). The imide protons associate with the vacancies to minimize the electrostatic and/or steric repulsion with the cations and thus become ordered as well. Recently, Balogh et al. also suggested the presence of such ordering interactions in

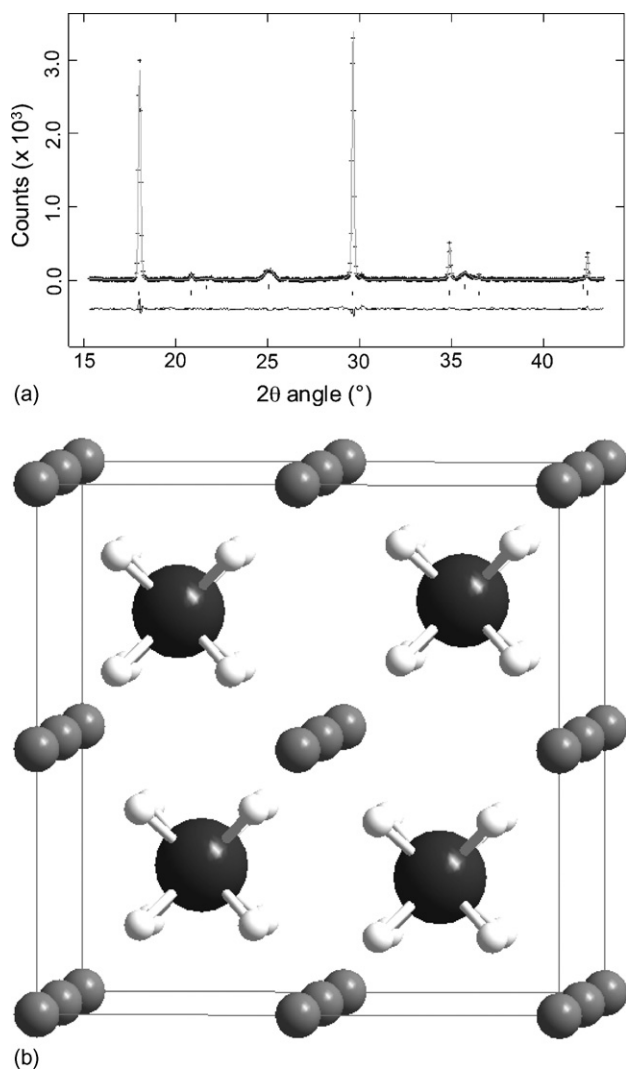


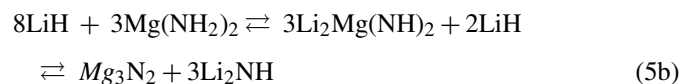
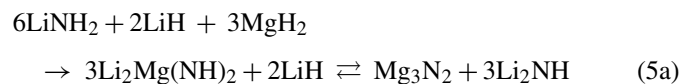
Fig. 10. (a) Rietveld refinement results of the in situ X-ray data for the model of  $\gamma$ - $\text{Li}_2\text{Mg}(\text{NH})_2$  in space group  $Fm\bar{3}m$ . Data (crosses), fitted profile (line), allowed Bragg reflections (tick marks) and difference curve (lower line) are shown. The fit includes both  $\text{MgO}$  (top tick marks) and  $\gamma$ - $\text{Li}_2\text{Mg}(\text{NH})_2$  (bottom tick marks). (b) Structure of  $\gamma$ - $\text{Li}_2\text{Mg}(\text{NH})_2$ . Nitrogen atoms (dark grey), protons (white), and mixed lithium, magnesium and vacancy sites (small grey) are shown. Note that although the imide protons are disordered, they are likely associated with the disordered cation vacancies that are also disordered.

the low temperature structure of  $\text{Li}_2\text{NH}$  [24]. In this case, one-eighth of the Li atoms are displaced from their tetrahedral sites to interstitial sites creating cation Frenkel defects (Fig. 11c). As in  $\alpha$ - $\text{Li}_2\text{Mg}(\text{NH})_2$ , the presence of vacancies drives an ordering of the surrounding imide protons. Such interactions also affect ordering in  $\text{LiNH}_2$ , in which half of the cation sites are vacant, driving the protons to orient themselves such that the N–H bonds are pointing between two vacant cation sites (Fig. 11d).

The structural similarities between  $\text{Li}_2\text{Mg}(\text{NH})_2$ ,  $\text{Li}_2\text{NH}$  and  $\text{LiNH}_2$  also suggest that the basic anti-fluorite structure might accommodate ratios of Li and Mg other than 2:1. For example, dehydrogenation of LiH,  $\text{LiNH}_2$  and  $\text{MgH}_2$  (or LiH and  $\text{Mg}(\text{NH}_2)_2$ ) mixed in the appropriate ratios yielded  $\text{Li}_{4-2x}\text{Mg}_x(\text{NH})_2$  ( $x=0.67$  and 0.5). In situ X-ray diffraction of both compositions indicated formation of a mix-

ture of  $\beta$ - $\text{Li}_2\text{Mg}(\text{NH})_2$  and  $\text{Li}_2\text{NH}$  at 220–250 °C (Fig. 12). As with  $\text{Li}_2\text{Mg}(\text{NH})_2$  ( $x=1$ ), rehydrogenation under 2000 psi (13.7 MPa)  $\text{H}_2$  at 220 °C yields  $\text{Mg}(\text{NH}_2)_2$ ,  $\text{LiNH}_2$  and LiH. The Li:Mg ratio of the  $\beta$ -phase could not be confirmed as exactly 2:1 because of the convolution of its diffraction pattern with that of  $\text{Li}_2\text{NH}$ . In these cases the ammonia related signals in the RGA appears at higher temperatures than the hydrogen signal. This is in marked contrast to the case for  $x=1$  (Li/Mg=2) in which the ammonia and hydrogen signals appeared simultaneously. The explanation for this observation will be discussed below.

As illustrated in (5a) and (5b), even off-stoichiometric starting ratios lead to the formation of  $\text{Li}_2\text{Mg}(\text{NH})_2$ : mixtures of  $6\text{LiNH}_2 + 2\text{LiH} + 3\text{MgH}_2$  (or  $8\text{LiH} + 3\text{Mg}(\text{NH}_2)_2$  as reported by Leng et al. [7]) form  $\beta$ - $\text{Li}_2\text{Mg}(\text{NH})_2$  and LiH at 220 °C before the reaction proceeds to form  $\text{Mg}_3\text{N}_2$  and  $\text{Li}_2\text{NH}$  above 300 °C (Fig. 13). This observation explains the two-step nature of the hydrogen desorption in this system:



The in situ diffraction experiments have yielded interesting clues to the mechanism of the hydrogen storage reaction. The formation of  $\text{Mg}(\text{NH}_2)_2$  and LiH upon hydrogenation instead of the original starting materials has been reported [8,10] and illustrates the greater stability of the latter combination of compounds. Luo and Sickafoose [10] have shown that a mixture of  $2\text{LiNH}_2$  and  $\text{MgH}_2$  heated at 220 °C under 10 MPa  $\text{H}_2$  (to prevent desorption and the formation of  $\text{Li}_2\text{Mg}(\text{NH})_2$ ) yields  $2\text{LiH} + \text{Mg}(\text{NH}_2)_2$ . Indeed, close scrutiny of our in situ XRD measurements on  $2\text{LiNH}_2$  and  $\text{MgH}_2$  immediately before hydrogen release revealed small peaks at  $2\theta=8.8^\circ$  and  $13.6^\circ$  which are indicative of  $\text{Mg}(\text{NH}_2)_2$  (Fig. 14). Although not shown in Fig. 14, peaks for LiH are briefly apparent as well. This interesting observation suggests that the mixture of  $2\text{LiNH}_2$  and  $\text{MgH}_2$  actually converts to  $2\text{LiH}$  and  $\text{Mg}(\text{NH}_2)_2$  first, and that the latter mixture is responsible for hydrogen release. Such an interpretation would explain why the dehydrogenation temperatures for the two mixtures ( $2\text{LiH} + \text{Mg}(\text{NH}_2)_2$  and  $2\text{LiNH}_2 + \text{MgH}_2$ ) are nearly identical despite the differences in the decomposition temperatures of the individual amines [26]. More detailed experiments will have to be performed to prove this idea conclusively.

The evolution of ammonia during hydrogen desorption has been reported by several groups and it has been suggested that ammonia is intimately involved in the hydrogen storage reactions [7,9,15]. It is stipulated that ammonia formed by the decomposition of the amide quickly reacts with LiH to release hydrogen [27]. This observation is supported by the delayed release of ammonia from compositions with larger initial amounts of LiH ( $x=0.67$  and 0.5 above). The presence of extra LiH consumes the ammonia until it has all been converted to an amide or imide. The reaction of  $\text{NH}_3$

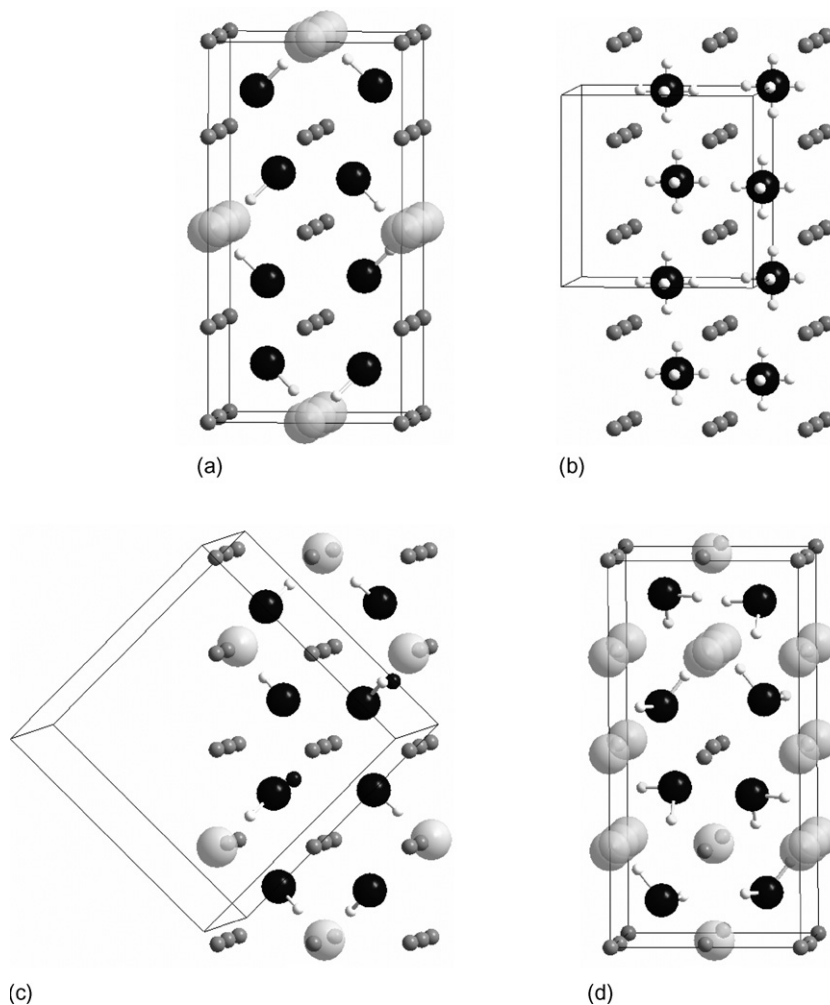


Fig. 11. Comparison of the structures of (a)  $\alpha$ - $\text{Li}_2\text{Mg}(\text{NH})_2$ , (b) high temperature cubic  $\text{Li}_2\text{NH}$ , (c) low temperature orthorhombic  $\text{Li}_2\text{NH}$  and (d)  $\text{LiNH}_2$ . Despite different symmetries and unit cells, the underlying structural similarities are striking. The association of the proton with the cation vacancies is evident in all but cubic  $\text{Li}_2\text{NH}$ , in which the protons are disordered. Nitrogen atoms (dark grey), protons (white), lithium and/or magnesium (small grey) and vacancies (large transparent grey) are shown.

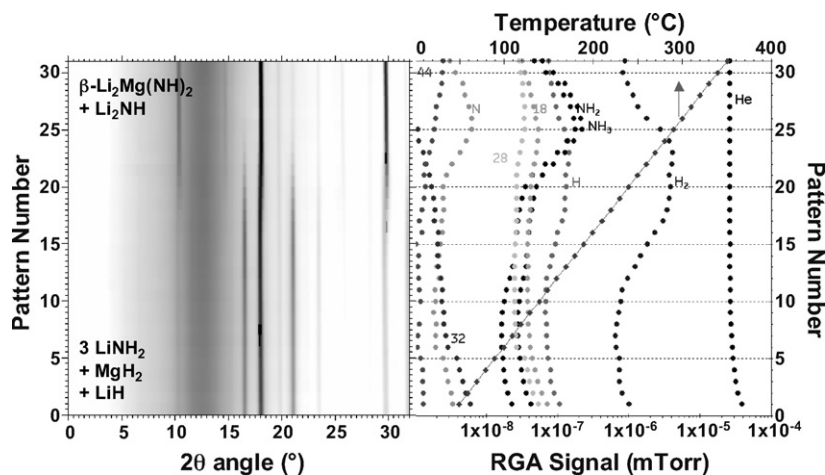


Fig. 12. In situ X-ray diffraction (left) and simultaneous RGA analysis of the evolved gases (right) during the first heating of a mixture of  $3\text{LiNH}_2 + \text{MgH}_2 + \text{LiH}$  to form a mixture of  $\beta$ - $\text{Li}_2\text{Mg}(\text{NH})_2$  and  $\text{Li}_2\text{NH}$ .

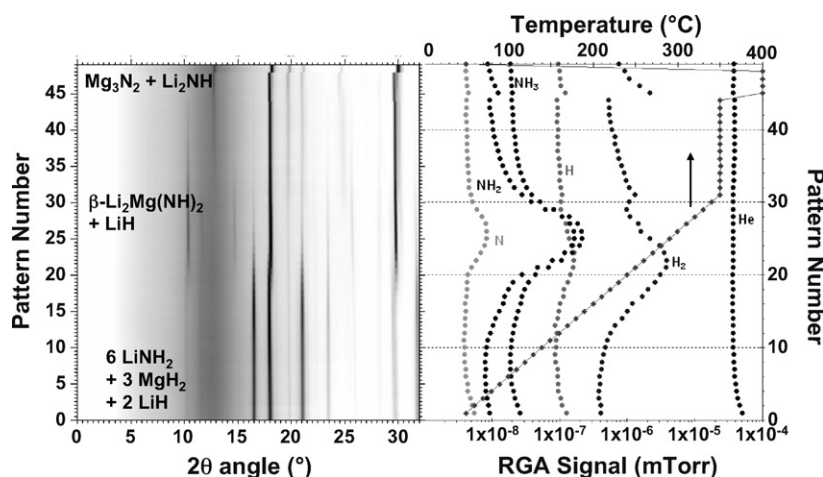


Fig. 13. In situ X-ray diffraction (left) and simultaneous RGA analysis of the evolved gases (right) during the first heating of a mixture of  $6\text{LiNH}_2 + 3\text{MgH}_2 + 2\text{LiH}$  to form a mixture of  $\beta\text{-Li}_2\text{Mg}(\text{NH})_2$  and  $\text{LiH}$ , followed by a mixture of  $\text{Mg}_3\text{N}_2$  and  $\text{Li}_2\text{NH}$ .

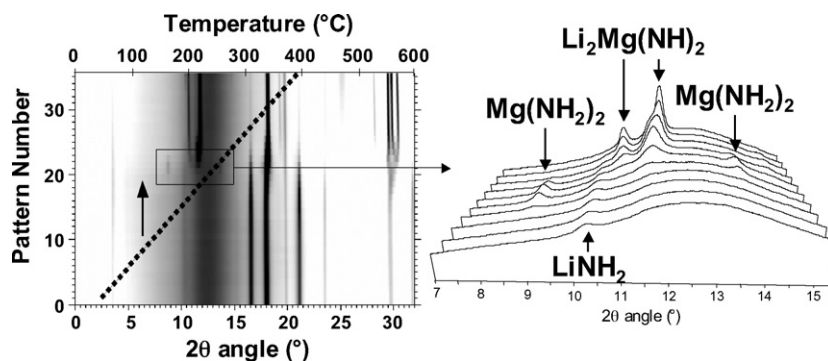


Fig. 14. In situ X-ray diffraction during the first heating of a mixture of  $2\text{LiNH}_2 + \text{MgH}_2$ . Close inspection of the diffraction patterns around the time of hydrogen desorption shows that  $\text{Mg}(\text{NH}_2)_2$  and  $\text{LiH}$  are formed before  $\alpha\text{-Li}_2\text{Mg}(\text{NH})_2$ .

with  $\text{MgH}_2$  is known to be much slower, which may explain the larger amount of ammonia released during the desorption from  $2\text{LiNH}_2 + \text{MgH}_2$  (1st decomposition) versus from  $\text{Mg}(\text{NH}_2)_2 + 2\text{LiH}$  (2nd decomposition). The loss of ammonia with each cycle is a major drawback of this system because it degrades the hydrogen storage capacity of the material over time and introduces into the hydrogen stream an impurity that is harmful to PEM fuel cells.

## 5. Conclusion

We have used a combination of synchrotron X-ray diffraction and neutron diffraction to determine the hydrogen storage reactions of mixtures of lithium amide and magnesium hydride. Dehydrogenation yields a mixed lithium and magnesium imide,  $\alpha\text{-Li}_2\text{Mg}(\text{NH})_2$ , with a unit cell twice that of  $\text{Li}_2\text{NH}$ . As the temperature is increased,  $\alpha\text{-Li}_2\text{Mg}(\text{NH})_2$  undergoes structural transitions to a primitive cubic structure followed by a face-centered cubic crystal structure. The transitions are the result of progressive disordering of the cations (Li and Mg) and the cation vacancies as the temperature is increased. A fourth, tetragonal structure is observed when desorption takes place under high hydrogen pressures. The multitude of structures observed in the  $\text{Li-Mg-N-H}$  system attests to the structural flexibility of these

imides that can accommodate significant numbers of vacancies while maintaining their basic anti-fluorite structure. The close relationship between the cation vacancy and the imide proton raises the interesting possibility that their interaction can have a structure directing effect: driving the formation of the Frenkel defect in  $\text{Li}_2\text{NH}$  and the vacancy ordering in  $\alpha\text{-Li}_2\text{Mg}(\text{NH})_2$  and  $\text{LiNH}_2$ . This effect will need further experimental clarification but cation, proton and vacancy interactions and migration are sure to be important factors in determining the hydrogen storage properties of these systems. The ability of these structures to accommodate large numbers of cation defects may provide a pathway to designing better hydrogen storage materials by cationic substitution at different ratios or with other elements. Ammonia release during hydrogen desorption in open (flow through) systems remains problematic for longevity and compatibility with PEM fuel cells.

## Acknowledgements

The authors acknowledge valuable technical assistance from Tom Raber at GE Global Research. We thank John Lemmon, Suchismita Sanyal, Grigori Soloveichik and J.C. Zhao at GE Global Research for valuable discussions and support. Parts of this material are based upon work supported by the U.S.

Department of Energy (DOE) under Award Number DE-FC36-05GO15062. We also thank Prof. Peter Stephens of SUNY Stony Brook for assisting the experiment at the SUNY X3 beamline of the National Synchrotron Light Source which was partially supported by the DOE under grant no. DE-FG02-86ER 45231. The work as NSLS X7B was supported under Contract DE-AC02-98CH10886 with the DOE, Office of Basic Energy Sciences, Chemical Sciences Division. Use of the National Synchrotron Light Source, Brookhaven National Laboratory, was supported by the DOE, Office of Science, Office of Basic Energy Sciences, under Contract No. DE-AC02-98CH10886.

## References

- [1] W. Grochala, P.P. Edwards, *Chem. Rev.* 104 (2004) 1283.
- [2] F.E. Pinkerton, B.G. Wicke, *Ind. Phys.* 10 (2004) 20.
- [3] P. Chen, Z. Xiong, J. Luo, J. Lin, K.L. Tan, *Nature* 420 (2002) 302.
- [4] P. Chen, Z. Xiong, J. Luo, J. Lin, K.L. Tan, *J. Phys. Chem.* 107 (2003) 10967.
- [5] F.W. Dafert, R. Miklausz, *Monatsh. Chem.* 31 (1910) 981.
- [6] W. Luo, *J. Alloys Compd.* 381 (2004) 284.
- [7] H.Y. Leng, T. Ichikawa, S. Hino, N. Hanada, S. Isobe, H. Fujii, *J. Phys. Chem. B* 108 (2004) 8763.
- [8] Z. Xiong, G. Wu, J. Hu, P. Chen, *Adv. Mater.* 16 (2004) 1522.
- [9] Y. Nakamori, G. Kitahara, S. Orimo, *J. Power Sources* 138 (2004) 309.
- [10] W. Luo, S. Sickafoose, *J. Alloys Compd.* 407 (2006) 274.
- [11] Z. Xiong, G. Wu, J. Hu, P. Chen, W. Luo, J. Wang, *J. Alloys Compd.* 417 (2006) 190.
- [12] Certain commercial materials and/or equipment are identified in this report to describe the subject adequately. Such identification does not imply recommendation or endorsement by the NIST, nor does it imply that the materials or/and equipment identified is necessarily the best available for the purpose.
- [13] A.P. Hammersley, ESRF Internal Report, ESRF98HA01T, FIT2D V9.129 Reference Manual V3.1, 1998.
- [14] P.J. Chupas, M.F. Ciruolo, J.C. Hanson, C.P. Grey, *J. Am. Chem. Soc.* 123 (2001) 1694.
- [15] T. Ichikawa, N. Hanada, S. Isobe, H.Y. Leng, H. Fujii, *J. Phys. Chem. B* 108 (2004) 7887.
- [16] The X-ray and neutron data of undeuterated  $\alpha$ -Li<sub>2</sub>Mg(NH)<sub>2</sub> were also collected and the analysis gave nearly identical results.
- [17] Jade 7.1.2, Materials Data Inc., Livermore, CA, 2004.
- [18] V. Favre-Nicolin, R. Černý, *J. Appl. Cryst.* 35 (2002) 734.
- [19] A.C. Larson, R.B. Von Dreele, General Structure Analysis System (GSAS), Los Alamos National Laboratory Report LAUR 86-748, 2000.
- [20] Data taken from Neutron News, vol. 3, no. 3, 1992, pp. 29–37 as tabulated at <http://www.ncnr.nist.gov/resources/n-lengths/>. The neutron scattering lengths (in fm) used in the refinements were −1.90 (Li), 5.375 (Mg), 6.671 (D), −3.739 (H), and 9.36 (N).
- [21] T. Noritake, H. Nozaki, M. Aoki, S. Towata, G. Kitahara, Y. Nakamori, S. Orimo, *J. Alloys Compd.* 393 (2005) 264.
- [22] K. Ohoyama, Y. Nakamori, S. Orimo, K. Yamada, *J. Phys. Soc. Jpn.* 74 (2005) 483.
- [23] R.D. Shannon, *Acta Crystallogr. A* 32 (1976) 751.
- [24] M.P. Balogh, C.Y. Jones, J.F. Herbst, L.G. Hector Jr., M. Kundrat, *J. Alloys Compd.* 420 (2006) 326.
- [25] *Fm-3m* is one of five possible space groups that cannot be distinguished based on systematic absences. The choice of space group is governed by the position(s) of the H/D atom, however the accurate determination of H atom positions is not possible based on the in-situ X-ray data and imperfect neutron data. The choice of *Fm-3m* with H atoms at the 32f position is considered the most sensible because it yields N–H bonds that point towards vacancies in the partially occupied cation sites, similar to the situation in the  $\alpha$  and  $\beta$  structures.
- [26] Y. Nakamori, G. Kitahara, A. Ninomiya, M. Aoki, T. Noritake, S. Towata, S. Orimo, *Mater. Trans.* 46 (2005) 2093.
- [27] Y.H. Hu, E. Ruckenstein, *J. Phys. Chem. A* 107 (2003) 9737.